

Theory of Magnetic Phase Diagrams in Hyperhoneycomb and Harmonic-honeycomb Iridates

Eric Kin-Ho Lee¹ and Yong Baek Kim^{1,2,3}

¹*Department of Physics and Center for Quantum Materials,
University of Toronto, Toronto, Ontario M5S 1A7, Canada.*

²*Canadian Institute for Advanced Research/Quantum Materials Program, Toronto, Ontario MSG 1Z8, Canada*

³*School of Physics, Korea Institute for Advanced Study, Seoul 130-722, Korea.*

(Dated: October 10, 2014)

Motivated by recent experiments, we consider a generic spin model in the $j_{\text{eff}} = 1/2$ basis for the hyperhoneycomb and harmonic-honeycomb iridates. Based on microscopic considerations, the effect of an additional bond-dependent anisotropic spin exchange interaction (Γ) beyond the Heisenberg-Kitaev model is investigated. We obtain the magnetic phase diagrams of the hyperhoneycomb and harmonic-honeycomb (\mathcal{H} -1) lattices via a combination of the Luttinger-Tisza approximation, single- \mathbf{Q} variational ansatz, and classical Monte Carlo simulated annealing. The resulting phase diagrams on both systems show the existence of incommensurate, non-coplanar spiral magnetic orders as well as other commensurate magnetic orders. The spiral orders show counter-propagating spiral patterns, which may be favorably compared to recent experimental results on both iridates. The parameter regime of various magnetic orders and ordering wavevectors are quite similar in both systems. We discuss the implications of our work to recent experiments and also compare our results to those of the two dimensional honeycomb iridate systems.

I. INTRODUCTION

Iridium-based compounds^{1–8} have spurred considerable interest because the interplay of strong atomic spin-orbit coupling (SOC), electronic correlations, crystal field effects, and sizable orbital overlaps in these compounds have been shown to give rise to exotic states of matter ranging from topological insulators to Weyl semimetals and quantum spin liquids.^{9–15} Drawing significant attention is the A_2IrO_3 family of layered honeycomb iridates^{4–7,16–32}: these materials were first described by the Kitaev model¹⁶ and later by the Heisenberg-Kitaev (HK) model¹⁸, both of which hosts a \mathbb{Z}_2 quantum spin-liquid ground state first discovered in the context of Kitaev’s exactly solvable spin-1/2 model.³³ Subsequently, similar exactly solvable spin models on several other two-dimensional (2D) and three-dimensional (3D) lattices were investigated.^{34–39}

Experimentally, the sodium honeycomb iridate— Na_2IrO_3 —has been shown to order magnetically in the zigzag phase^{5,7,21}, while the lithium counterpart— Li_2IrO_3 —is believed to also order magnetically but in a different ground state.³² The quest to find an appropriate minimal model that can explain the observed orders, low energy excitations, as well as bulk thermodynamic properties has been actively pursued. To address these points, localized pseudospin models involving exchanges in addition to the Heisenberg and Kitaev couplings have been considered, including the symmetry-allowed off-diagonal exchange^{40–42}, further neighbour exchanges^{19,43}, and distortion-induced anisotropies^{41,42}. Electronic band structure calculations^{24,25,27,44} have also been investigated to further our understanding of these compounds. Indeed, a suitable minimal model may predict the behaviour of these layered honeycomb iridates under a variety of perturbations and may direct us to the discovery of exotic physics, including the illusive quantum spin liquid phase.

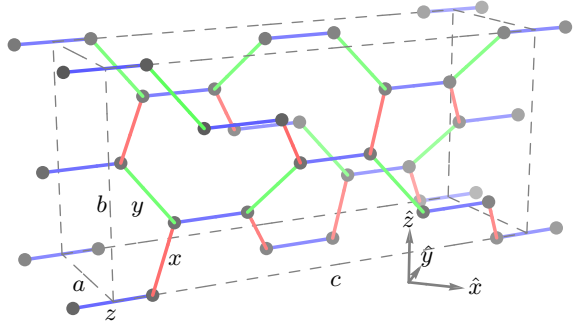
Recently, two three-dimensional polymorphs of the layered honeycombs with chemical formula Li_2IrO_3 have been discovered, fuelling intrigue over the family of honeycomb-

based iridate compounds. Curiously, these two materials—the hyperhoneycomb (\mathcal{H} -0)⁴⁵ and harmonic-honeycomb (\mathcal{H} -1)⁴⁶—behave rather similarly: they have the same stoichiometry as the layered honeycomb with analogous three-dimensional crystal structures, they order magnetically with no net moment at similar temperatures (~ 38 K), and their magnetization curves behave non-linearly at low fields. Furthermore, thermodynamic measurements^{45,46} suggested that both 3D iridates might order unconventionally in a non-collinear fashion and recent single-crystal resonant magnetic x-ray diffraction experiments^{47,48} find a complex incommensurate structure with non-coplanar and counter-propagating moments in both iridates. Indeed, with the discovery of these two 3D honeycomb compounds and to build on past work in both the intermediate-coupling regime⁴⁹ and localized^{37,50–55} limits, the search for a relevant minimal model to describe the family of honeycomb iridates has now become more fascinating. Can the same minimal model describe both the 2D and 3D honeycomb iridates while capturing the similarities and heterogeneity amongst these compounds? In this work, driven by the fact that these compounds have similar local structures, we suggest that the nearest-neighbor J - K - Γ model, which was recently used to describe the layered honeycomb iridates⁴⁰, is a good starting point in the discussion of this family of compounds, especially in regards to the magnetic order.

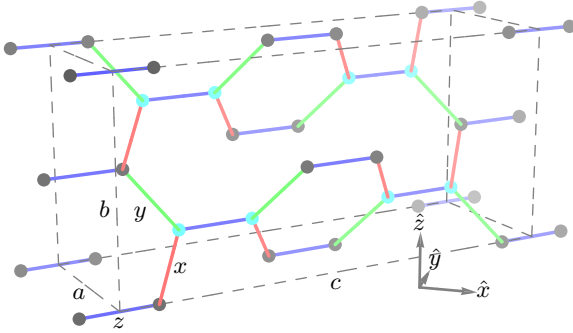
The rest of the paper is organized as follows. We begin, in Sec. II, by discussing the hyperhoneycomb and \mathcal{H} -1 lattices, drawing special attention to the similarities and differences between these three-dimensional analogues of the honeycomb lattice. In Sec. III, we describe the minimal effective model of $j_{\text{eff}} = 1/2$ pseudospins that describes the low-energy physics of the hyperhoneycomb and \mathcal{H} -1 lattices in the Mott insulating limit. The presence of the off-diagonal exchange term, Γ , along with the familiar Heisenberg and Kitaev terms, is shown to be necessary from a strong-coupling expansion of the underlying, multi-band electronic model. Following this, in Sec. IV we present the classical phase diagram of these models us-

ing a combination of Luttinger-Tisza approximation, single- \mathbf{Q} ansatz minimization, and simulated annealing. We show that the hyperhoneycomb and \mathcal{H} -1 lattices have similar phase diagrams, but differ from the phase diagram of the 2D honeycomb iridates in important ways. In addition to analogues of the ferromagnetic, antiferromagnetic, zigzag, and stripy phases of the HK model, we find a number of non-coplanar, counter-propagating spiral phases, multiple- \mathbf{Q} states, as well as phases that have no direct analogues in the HK-limit. We expound these phases and their static structure factors in Sec. V, thus providing results that can be compared with experiments. Finally, in Sec. VI, we discuss the relevance of our results to the newly discovered 3D-Li₂IrO₃ compounds.

II. STRUCTURE OF HYPERHONEYCOMB AND \mathcal{H} -1 LATTICES



(a) Hyperhoneycomb lattice



(b) \mathcal{H} -1 lattice

FIG. 1. (Color online) Ideal iridium ion network in the hyperhoneycomb and \mathcal{H} -1 lattices. The x , y , and z bonds are colored red, green, and blue, respectively. The bridging-sites are colored cyan in Fig. 1b, and the z -bonds connecting adjacent bridging-sites are the bridging- z -bonds. The gray dashed boxes are the conventional unit cells. The conventional lattice vectors— a , b , and c —are marked accordingly.

The ideal iridium ion (Ir) network in the hyperhoneycomb (Fig. 1a) and \mathcal{H} -1 (Fig. 1b) lattices share many common features but also have some important differences. In this section,

we highlight these main points and introduce conventions relevant to the description of the magnetic phases explored in Sec. V.

The conventional unit cells of both hyperhoneycomb and \mathcal{H} -1 lattices are orthorhombic with the former being face-centered⁴⁵ and the latter being base-centered⁴⁶. The hyperhoneycomb primitive unit cell has four Ir while the \mathcal{H} -1 primitive unit cell has eight; hence, the conventional unit cell of hyperhoneycomb contains four primitive units while in the \mathcal{H} -1, there are two. In our chosen coordinate system, the conventional lattice vectors of both hyperhoneycomb and \mathcal{H} -1 lattices are given by the orthorhombic set $\mathbf{a} = (-2, 2, 0)$, $\mathbf{b} = (0, 0, 4)$, and $\mathbf{c} = (6, 6, 0)$. All the Ir sites reside in their respective oxygen octahedra and these octahedra share edges between NN Ir sites.

The Ir sites are three-fold coordinated, with the three NN bonds labelled as x , y , and z as illustrated in Figs. 1a and 1b. In the coordinate system that we have chosen, the label represents the direction to which the bond is normal. For example, the sites joined by an x -bond form either the vector $(0, 1, 1)$ or $(0, 1, -1)$. We will see that this labelling scheme is also used in describing the low-energy Hamiltonian of these lattices in Sec. III.

The hyperhoneycomb (also known as the \mathcal{H} -0) and \mathcal{H} -1 lattices have been described as strips of layered honeycombs joined in an ABAB fashion along the \hat{c} direction. The A and B strips are mirrored copies of each other and are hence related by glide planes.^{46,54} In the \mathcal{H} - n notation, n refers to the number of rows of hexagons in the each of the honeycomb strips. For the hyperhoneycomb lattice, $n = 0$ indicates that no complete hexagons are present. For the \mathcal{H} -1 lattice, each honeycomb strip is one row in width. Despite the difference in the topology of the Ir network, the projection along the conventional planes (ab , ac , and bc planes) are identical between the two lattices.

We define a *honeycomb-plane* associated with every site: it is the plane that is spanned by the site's three NN bonds. Alternatively, it can be defined as the plane that contains the honeycomb strip to which the site belongs. Since the honeycomb strips are related by glide planes, there are only two orientations that honeycomb-planes can take. The honeycomb-planes are important when discussing the magnetic orders in Sec. V, especially for the spiral phases.

All Ir are symmetry-equivalent in the hyperhoneycomb lattice, but in the \mathcal{H} -1 lattice, there are two inequivalent sets. These two inequivalent sets of Ir in the \mathcal{H} -1 lattice can be classified by considering whether the site shares the same honeycomb-plane with all its NNs. We denote the sites that don't share the same honeycomb-plane with all its NNs as *bridging-sites* since they connect the A and B honeycomb strips. Consequently, we call the z -bonds that connect bridging-sites *bridging- z -bonds*, while the other symmetry-inequivalent z -bonds *non-bridging- z -bonds*. This terminology is used in the discussion of the spin patterns in several of the magnetic orders.

III. $j_{\text{eff}} = 1/2$ GENERIC PSEUDOSPIN MODEL

In compounds containing Ir^{4+} ions residing in oxygen octahedral crystal fields, the combination of large atomic spin-orbit coupling and strong electronic correlations can result in low-energy physics describable by highly anisotropic $j_{\text{eff}} = 1/2$ pseudospin models (hereafter, we will use *spin* and *pseudospin* interchangeably for brevity).^{16,40,56,57} When the bonds are comprised of edge-shared octahedra, such as the NN bonds found in both the hyperhoneycomb and the \mathcal{H} -1 lattices, a symmetric off-diagonal exchange term—denoted by Γ —is generically present in addition to the Heisenberg and Kitaev exchange terms.^{40–42} As such, a minimal Hamiltonian that describes the low-energy physics of these systems can be written as

$$H = \sum_{\langle i,j \rangle \in \alpha\beta(\gamma)} \left[J \mathbf{S}_i \cdot \mathbf{S}_j + K S_i^\gamma S_j^\gamma \pm \Gamma \left(S_i^\alpha S_j^\beta + S_i^\beta S_j^\alpha \right) \right], \quad (1)$$

where \mathbf{S}_i is the $j_{\text{eff}} = 1/2$ pseudospin at site i , the summation is over NN bonds $\langle i, j \rangle$ labelled by $\gamma \in (x, y, z)$, and $\langle i, j \rangle \in \alpha\beta(\gamma)$ is shorthand for $\langle i, j \rangle \in \gamma, \alpha \neq \beta \neq \gamma$. The \pm sign in front of Γ is a reminder that, unlike the J and K terms, the Γ term can have relative minus signs on different bonds. The sign structures of Γ for both the hyperhoneycomb and \mathcal{H} -1 lattices are shown in Fig. 8 (see Appendix B for details on the choice of the Γ sign structure).

The exchange interactions J , K , and Γ can be obtained microscopically via a strong coupling expansion of a t_{2g} multi-band tight-binding model with on-site interactions and large atomic SOC. The details can be found in Appendix A and Ref. 40. Here we summarize the exchange interactions' dependence on the parameters of the multi-band Hubbard model, which include Coulomb repulsion U , Hund's coupling J_H , spin-orbit coupling λ , and three t_{2g} hopping amplitudes denoted by t_1 through t_3

$$J = \frac{4}{27} \left[\frac{(2t_1 + t_3)^2 (4J_H + 3U)}{U^2} - \frac{16J_H(t_1 - t_3)^2}{(2U + 3\lambda)^2} \right] \\ K = \frac{32J_H}{9} \left[\frac{(t_1 - t_3)^2 - 3t_2^2}{(2U + 3\lambda)^2} \right], \quad \Gamma = \frac{64J_H}{9} \frac{t_2(t_1 - t_3)}{(2U + 3\lambda)^2}. \quad (2)$$

We note that all three exchange interactions are present at this order of perturbative expansion and that the presence of Hund's coupling J_H is needed for a finite K and Γ . Furthermore, the signs of the exchange interactions sensitively depend on relative magnitudes and signs of t_1 through t_3 , which themselves are functions of Slater-Koster amplitudes⁵⁸ that parametrize t_{2g} orbital overlaps and oxygen-iridium orbital overlaps (details can be found in Appendix A and Ref. 40). Generically, this sensitivity implies that all the phases we find are potentially experimentally relevant to the 3D-Li₂IrO₃ compounds.

IV. CONSTRUCTION OF PHASE DIAGRAMS

The NN $j_{\text{eff}} = 1/2$ pseudospin Hamiltonian in Eq. 1 describes the local, low-energy physics of the hyperhoneycomb and \mathcal{H} -1 lattices in the strong SOC and electron correlation limit. Unlike the 2D honeycomb iridates, both the hyperhoneycomb and the \mathcal{H} -1 lattices are three-dimensional, thus making numerical techniques for quantum spin models, such as exact diagonalization and density matrix renormalization group, challenging to implement. This is further exacerbated by the large unit cells in these 3D lattices: compared to the two Ir ions in the 2D-honeycomb lattice's primitive unit cell, there are four and eight Ir ions in the primitive unit cell for the hyperhoneycomb and \mathcal{H} -1 lattices, respectively.

Although these numerical issues in the quantum analysis are difficult to overcome, a classical understanding of these three-dimensional pseudospin models is both important and relevant inasmuch that the hyperhoneycomb and \mathcal{H} -1 iridates are believed to be magnetically-ordered.^{45,46} A classical analysis may be sufficient since, in the 2D-honeycomb pseudospin model, the classical phase diagram well-approximated the magnetic phases found via exact diagonalization.^{18,31,40,59} Furthermore, quantum fluctuations—the key ingredient in generating exotic, non-classical phases—are generally believed to be suppressed in 3D systems compared to 2D systems. To this end, we analyze the $j_{\text{eff}} = 1/2$ pseudospin Hamiltonians of both hyperhoneycomb and \mathcal{H} -1 lattices in the classical limit using a combination of the Luttinger-Tisza approximation^{60,61}, single- \mathbf{Q} ansatz minimization, and classical Monte Carlo simulated annealing.

A. Methods

In the Luttinger-Tisza approximation (LTA),^{60,61} the local constraint of $|S_i| = 1$ is relaxed to a global constraint $\sum_i |S_i| = N$. The lowest energy configuration satisfying the global constraint can be easily solved in momentum space. This configuration is then checked against the local constraint: if it is satisfied, then the LTA succeeded in finding the exact classical ground state; otherwise, the LTA failed but has instead found a lower bound of the ground state energy. In the parameter regions where LTA failed, we implemented a combination of single- \mathbf{Q} ansatz minimization and classical Monte Carlo simulated annealing to find the classical ground state configuration.

In the single- \mathbf{Q} ansatz minimization, an upper bound to the classical energy is determined variationally by a trial spin configuration of the form

$$\mathbf{S}_a(\mathbf{r}_i) = \hat{\mathbf{e}}_a^z \cos \alpha_a + \sin \alpha_a [\hat{\mathbf{e}}_a^x \cos(\mathbf{Q} \cdot \mathbf{r}_i) + \hat{\mathbf{e}}_a^y \sin(\mathbf{Q} \cdot \mathbf{r}_i)], \quad (3)$$

where $\mathbf{S}_a(\mathbf{r}_i)$ is the pseudospin on sublattice a in the (conventional) unit cell \mathbf{r}_i , $\hat{\mathbf{e}}_a^i$ is an orthonormal set of vectors defining a local frame for sublattice a , α_a is the canting angle for sublattice a , and \mathbf{Q} is the \mathbf{Q} -vector common to all sublattices. The energy of this ansatz is minimized to find a variational bound to the classical ground state energy. Since the wavevec-

tors \mathbf{Q} and $\mathbf{Q}' \equiv \mathbf{g} \pm \mathbf{Q}$ (where \mathbf{g} is a reciprocal lattice vector) parametrize the same set of spin configurations, we can restrict the domain over which minimization of \mathbf{Q} is performed to the first Brillouin zone.

Classical simulated annealing using the single-spin Metropolis algorithm and periodic boundary conditions was performed in conjunction with the single- \mathbf{Q} ansatz minimization. Simulated annealing has the advantage over single- \mathbf{Q} ansatz minimization in that it can access states that are characterized by multiple \mathbf{Q} -vectors and is less prone to being trapped by local minima in energy. On the other hand, although simulated annealing can access single- \mathbf{Q} states given by Eq. 3, the allowable \mathbf{Q} -vectors must be commensurate with the finite system sizes chosen in our simulations. A saw-tooth like temperature annealing profile was used to better traverse the spin-configuration space and a minimum of 1×10^6 sweeps (updates per spin) were used for each simulation.

Over 8000 (J, K, Γ) parameter points for each lattice were analyzed, with particular focus on spiral phases. For each parameter point, simulated annealing was performed with random initial conditions on systems with $n \times n \times n$ conventional unit cells where $n \leq 10$. For the spiral regions, we performed additional annealing on systems with $m \times 1 \times 1$ conventional unit cells, where $m \leq 100$ is the direction along the spiral wavevector. In addition, a minimum of 1000 single- \mathbf{Q} ansatz minimization runs were also performed per parameter point. The minimum energy amongst these simulated annealing and single- \mathbf{Q} ansatz minimization runs is deemed the variational bound of the ground state energy and the corresponding pseudospin configuration is used to characterize the magnetic order of the ground state at that parameter point.

B. General considerations

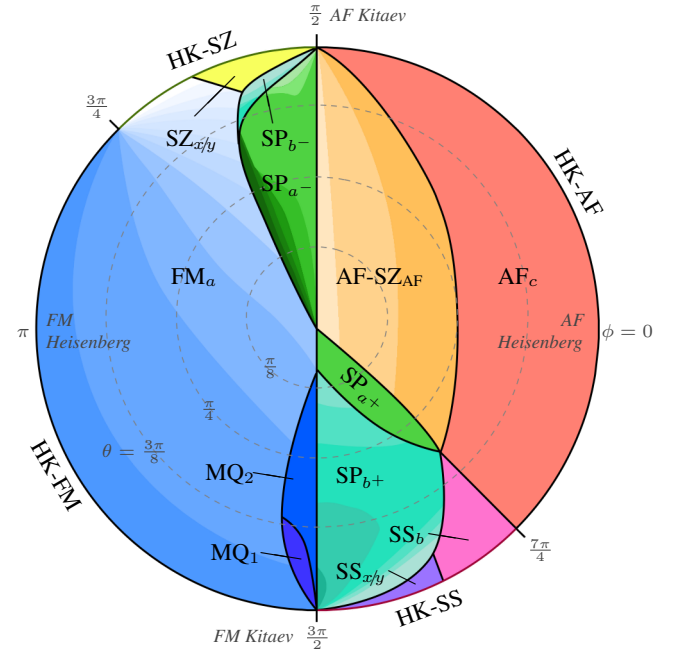
Before delving into the details of the classical magnetic ground states of Eq. 1, we first examine some general features of the hyperhoneycomb and \mathcal{H} -1 phase diagrams, which were obtained via the methods outlined in Sec. IV A.

To fix the overall energy scale, we parametrize the (J, K, Γ) parameter space using an angular representation

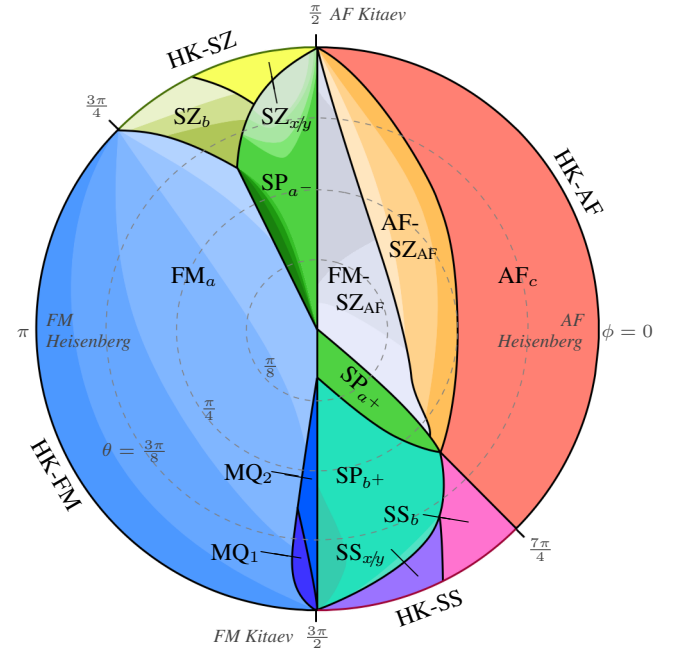
$$(J, K, \Gamma) = (\sin \theta \cos \phi, \sin \theta \sin \phi, \cos \theta), \quad (4)$$

such that $\sqrt{J^2 + K^2 + \Gamma^2} = 1$. The phase diagrams are plotted as polar plots, where the angular component is given by ϕ and the radial component, r , is given by θ . In Figs. 5a and 5b, we show the phase diagrams for the hyperhoneycomb and \mathcal{H} -1 lattices, respectively, when $\Gamma \geq 0$ (i.e. $\phi \in [0, 2\pi)$ and $r = \theta \in [0, \frac{\pi}{2}]$); the $\Gamma \leq 0$ results can be obtained by applying time-reversal on the odd sublattice pseudospins, which transforms $(J, K, \Gamma) \rightarrow (-J, -K, -\Gamma)$ and can be seen in Fig. 5. Prior to Sec. V C, we will concentrate on the $\Gamma \geq 0$ case with the understanding that equivalent statements can be made for the $\Gamma \leq 0$ case. Important properties of the $\Gamma \leq 0$ phases—especially those relating to experimental results—will be discussed in Sec. V C.

At first glance, we note the striking similarities between the two phase diagrams: despite the different topology of the hy-



(a) Hyperhoneycomb model



(b) \mathcal{H} -1 model

FIG. 2. (Color online) Classical phase diagrams for the J - K - Γ pseudospin model with $\Gamma \geq 0$. The parametrization of the exchange interactions can be found in Eq. 4. A detailed description of the phases can be found in Sec. V while a summary can be found in Table I. The color contours are guides for the eye: in the case of spiral (SP) states, they represent the length of the \mathbf{Q} -vector, whereas in the case of non-spiral states, they represent properties relevant to that particular phase; see Sec. V for details.

perhoneycomb and \mathcal{H} -1 lattices, the parameter regimes where we find the various magnetic orders and phase boundaries are similar in both systems. This notable result emphasizes the commonalities shared between the two systems as far as local physics is concerned. On the other hand, when compared to the classical phase diagram of the 2D honeycomb iridate from Ref. 40, we notice that the zigzag region has reduced in size and the spiral phases have become more prevalent. In particular, the 120° phase of the 2D model is now a spiral phase in the two 3D models.

On the outer edges of the two phase diagrams, Γ vanishes and the Hamiltonians reach the isotropic HK limit. With increasing ϕ , we encounter the Néel (HK-AF), skew-zigzag (HK-SZ), ferromagnet (HK-FM), and skew-stripy phases (HK-SS), which were discussed in the context of the 2D-honeycomb and 3D-honeycomb iridates.^{18,50,51,54,62,63} When $\Gamma = 0$, the classical ground state manifold possesses an emergent $SU(2)$ symmetry despite the presence of SOC. However, both classical and quantum order-by-disorder (ObD) lift this emergent degeneracy and choose particular spatial directions for the moments.^{18,50,51,63} Indeed, finite Γ also breaks the emergent symmetry⁴⁰ and pins pseudospin moments in particular spatial directions, causing the phases on the inside of the phase diagram to be non-collinear in general.

In the HK limit, the four-sublattice transformation^{18,64,65} exactly maps the parameter point (J, K) to $(-J, K - 2J)$ even in the quantum limit for both the hyperhoneycomb^{50,51} and \mathcal{H} -1⁵⁴ systems, thus relating the left and right edges of the phase diagram. In the presence of finite Γ , however, the four-sublattice transformation is not longer useful (it does not map a parameter point with finite Γ to another point within the phase diagram); the left and right *interiors* of the phase diagrams are no longer related.

The centers of the phase diagrams are the Γ -only points. These points, much like in the 2D-honeycomb case, possess highly degenerate ground state manifolds.⁴⁰ Therefore, similar to the Kitaev points, small perturbations can drive different magnetic orders. As a result, we see that a number of phases converge at these highly-degenerate points.

C. Presence of new magnetic orders

The effects of a finite Γ is most pronounced near the Kitaev points where the highly degenerate classical ground state manifolds can be lifted by small perturbations. As a result, finite Γ in these regions generates new magnetic orders that are not continuously connected with those found along the HK limit. Of the eight new magnetic orders, four are incommensurate spiral phases (SP_{a-} , SP_{a+} , SP_{b+} , and SP_{b-}), two are multiple- \mathbf{Q} states (MQ_1 and MQ_2), one is an antiferromagnetic state (AF-SZ_{AF}), and one has finite net moment (FM-SZ_{AF}). Of the four spiral states, two possess \mathbf{Q} -vectors that vary in length depending on the ratio of the exchange parameters while all of them contain counter-propagating spiral patterns (see Sec. V for details).

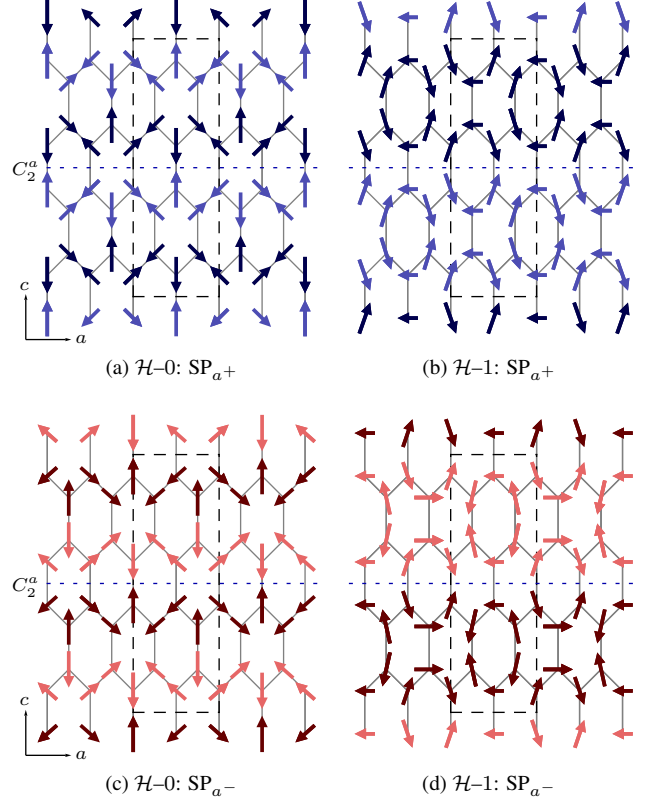


FIG. 3. (Color online) Real-space spin configurations of the SP_a spiral states obtained from simulated annealing with spins projected on to the ac -plane. The chosen parameter points yield $\mathbf{Q} = (0.33, 0, 0)$; however, we note that the \mathbf{Q} -vector in these phases are generally incommensurate and are not the same as the peak positions of the structure factor (see main text and Figs. 9, 10). The black dashed boxes enclose the conventional unit cells. Identical colors indicate that the sublattices share spiral-planes. Shades of blue indicate that the spiral-planes are aligned with the honeycomb-planes while shades of red indicate that the spiral-planes are not aligned with the honeycomb-planes. The handedness of adjacent sites can be readily verified as being opposite: the spirals counter-propagate. Examples of the preserved rotation symmetry are indicated by the dotted blue lines.

D. Magnetic orders continuously connected to the Heisenberg-Kitaev limit

Away from the Kitaev points, finite but small Γ modifies existing magnetic orders found in the HK limit. Several of the existing phases—namely the HK-SZ, HK-FM, and HK-SS phases—continuously deform with increasing Γ to acquire additional spin textures. The details of these additional spin textures depend on the particular lattice in consideration, which we will outline in Sec. V.

V. DESCRIPTION OF THE MAGNETIC ORDERS

In this section, we provide detailed descriptions of the magnetic phases found in our phase diagrams. We first discuss the

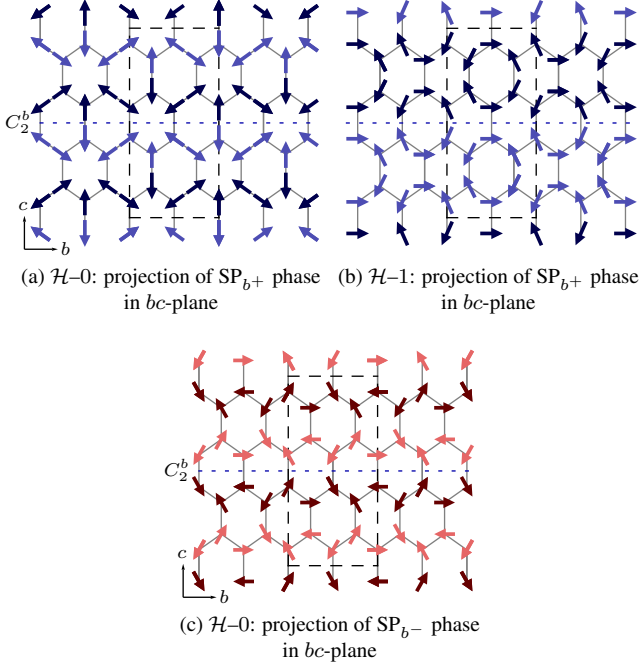


FIG. 4. (Color online) Real-space spin configurations of the SP_b spiral states obtained from simulated annealing with spins projected on to the bc -plane. The chosen parameter points yield $\mathbf{Q} = (0, 0.33, 0)$; however, we note that the \mathbf{Q} -vector in these phases are generally incommensurate. See caption in Fig. 3 for further details. In the case of the SP_{b-} phase, only the spiral planes and not the spins preserve the C_2^b rotation symmetry.

new magnetic orders, then we will describe the phases that are continuously connected with those at the HK limit. We also present the static structure factors of the spiral phases, which are relevant to x-ray and neutron scattering experiments. A summary of the phases discussed in this section can be found in Table I.

A. Emergent magnetic orders

Spiral orders: The spiral phases are those that can be represented by the ansatz in Eq. 3 with incommensurate \mathbf{Q} -vectors. They are located where the Kitaev exchange dominates over the Heisenberg exchange and where the two exchanges compete and have opposite signs. These spiral regions are connected to both the Kitaev and the pure- Γ points and border the $J = 0$ line. The above description of the location of spirals states is valid for both $\Gamma \geq 0$ and $\Gamma \leq 0$.

There are three spiral phases shared by both lattices: SP_{a+} , SP_{a-} , and SP_{b+} . In addition, SP_{b-} is found in the hyperhoneycomb lattice in a small region near the SP_{a-} phase. All these spiral phases do not have a net moment and they are all non-coplanar.

In the FM Heisenberg-AF Kitaev region (quadrant II of Fig. 2), we find the SP_{a-} phase. This phase has a \mathbf{Q} -vector of the form $(h00)$ (in the orthorhombic hkl notation), signifying that

the spirals run along the \hat{a} direction; therefore, we label this state as SP_{a-} . In the hyperhoneycomb lattice, there is also the nearby SP_{b-} phase, which has a \mathbf{Q} -vector of the form $(0k0)$.

In the AF Heisenberg-FM Kitaev region (quadrant IV), there are two spiral phases: the smaller region has a \mathbf{Q} -vector of the form $(h00)$ while the larger region has $(0k0)$. We label the former SP_{a+} and the latter SP_{b+} .

We illustrate an example of the real-space spin configuration for these phases in Figs. 3 and 4 using relevant projections that highlight the spin spirals. For the SP_a phases, the spins have been projected on to the ac plane while, for the SP_b phases, the projection is on to the bc plane. Although we have chosen parameter points that give commensurate \mathbf{Q} -vectors, we note that generically the phases are incommensurate spiral phases.

Prior to expounding the features of these spiral states, we emphasize that the quoted \mathbf{Q} -vectors are those that would appear in the single- \mathbf{Q} ansatz of Eq. 3, which are defined up to reciprocal lattice vectors of the conventional Brillouin zone. We stress that these \mathbf{Q} -vectors are related, but not necessarily the same as, the peak positions of the static structure factor, which we denote by \mathbf{q} . The static structure factor is given by

$$\begin{aligned} S(\mathbf{q}) &= \frac{1}{N} \sum_{ij} \langle \mathbf{S}_i \cdot \mathbf{S}_j \rangle e^{-i\mathbf{q} \cdot (\mathbf{r}_i - \mathbf{r}_j)} \\ &= \frac{1}{N} \sum_{ab} \langle \mathbf{s}_a^{ab} \rangle e^{-i\mathbf{q} \cdot \mathbf{r}_{ab}}, \end{aligned} \quad (5)$$

where \mathbf{S}_i is the spin at site i of the ground state configuration and \mathbf{r}_i is its real-space position. In the second line, we summed over the unit cells but retained the sublattice indices such that the static structure factor is written in terms of the matrix spin-spin structure factor $\mathbf{s}_a^{ab} = \mathbf{S}_a^a \cdot \mathbf{S}_{-a}^b$ and relative sublattice positions $\mathbf{r}_{ab} = \mathbf{r}_a - \mathbf{r}_b$. In this second form, we see explicitly that single- \mathbf{Q} ansatz can have peaks at $\mathbf{q} = \mathbf{g} \pm \mathbf{Q}$ where \mathbf{g} is a reciprocal lattice vector of the conventional Brillouin zone (one of the form (hkl) where all indices are integers). However, because of the form factor $e^{-i\mathbf{q} \cdot \mathbf{r}_{ab}}$ and the matrix structure of \mathbf{s}_a^{ab} , not all peaks will have the same intensity and some may even be extinguished.

In Figs. 9 and 10, we show the static structure factors along relevant cuts in reciprocal space which highlights the difference between \mathbf{Q} and \mathbf{q} . Although the shown SP_a phases have the same $\mathbf{Q} = (0.33, 0, 0)$, SP_{a-} possesses a peak at $\mathbf{q} = [(100) - \mathbf{Q}] = (0.66, 0, 0)$ while SP_{a+} does not. Instead, SP_{a+} possesses a peak at $\mathbf{q} = [(100) + \mathbf{Q}] = (1.33, 0, 0)$. Likewise for the SP_b phases: SP_{b-} and SP_{b+} differ in that SP_{b-} possesses a peak at $\mathbf{q} = [(010) - \mathbf{Q}]$ while the closest peak along the $(0k0)$ direction for SP_{b+} is located at $\mathbf{q} = [(010) + \mathbf{Q}]$. This property is generic for all \mathbf{Q} -vectors encountered in the spiral phases and hence explain our chosen notation: the spiral phase $SP_{x\pm}$ possesses the lowest-order structure factor peak at $\mathbf{q} = (\mathbf{1}_x \pm \mathbf{Q})$, where $\mathbf{1}_x$ is short form for (100) or (010) depending on whether x is a or b . This result is correlated with the orientation of the *spiral-planes* of these phases, which we will address after introducing several properties of these spiral-planes.

Although these are non-coplanar spirals, spins on any given

sublattice all lie in the same plane, which we term *spiral-plane* of the sublattice/site (this may not be evident in Figs. 3 and 4 due to the projections). In other words, the non-coplanar nature of these spiral phases is due to different sublattices having different spiral-planes. Specifically, sublattices that share honeycomb-planes also share spiral-planes,⁶⁶ whereas sublattices that don't share honeycomb-planes have spiral-planes related by symmetry: in the SP_a phases, both the spiral-planes and spins preserve the C_2 rotation symmetry about the \hat{a} direction (hereby denoted as C_2^a), while in the SP_{b+} phase, both the spiral planes and spins preserve the C_2^b rotation symmetry. In SP_{b-} , the spins break all C_2 symmetries but the spiral-planes are related by the C_2^b rotations. In Figs. 3 and 4, sites that have the same spiral-planes have the same color. We have also illustrated the preserved symmetry operations.

Despite possessing the same \mathbf{Q} -vector for each sublattice as evident in Eq. 3, NNs that share spiral-planes have spirals that propagate with different handedness, which can be readily verified in Figs. 3 and 4. In other words, the angles formed by NN spins that share spiral-planes are not constant as the spiral propagates—we say that the two spirals *counter-propagate*. We note that the corresponding spiral phases in the $\Gamma \leq 0$ regime also possess counter-propagating spirals. This is because the time-reversal operation on odd sublattices leaves the handedness of all spirals invariant.

The orientations of the spiral-planes are related to the honeycomb planes and distinguish the + from the − phases. They are also correlated with the positions of the peaks in the structure factors. In both the SP_{b+} and SP_{a+} phase, the spiral-planes at each site is aligned with the honeycomb-plane of that site. On the other hand, in the SP_{a-} and SP_{b-} phases, the spiral-planes at each site is aligned with the other honeycomb-plane of the lattice.⁶⁷ This implies that states that have structure factor peaks at $\mathbf{q} = (\mathbf{1}_x \pm \mathbf{Q})$ have honeycomb-planes aligned/not aligned with spiral planes. In Fig. 3 and 4, we illustrate the alignment of the spiral-planes and the honeycomb-planes by the hue of the sites: shades of blue indicates that the site's spiral-plane and honeycomb-plane are in alignment, shades of red indicate otherwise.

The lengths of the \mathbf{Q} -vectors are illustrated as a guide for the eye by color contours in Fig. 2: the \mathbf{Q} -vectors lengthen from the lightest to the darkest of colors within each phase. In the SP_{a+} and SP_{b-} phases, the \mathbf{Q} -vectors are approximately constant at $(0.33, 0, 0)$ and $(0, 0.33, 0)$, respectively. On the other hand, the \mathbf{Q} -vector varies continuously within the SP_{a-} and SP_{b+} phases.

In the SP_{a-} phase of the hyperhoneycomb lattice, the \mathbf{Q} -vector varies between approximately $(0.20, 0, 0)$ and $(0.47, 0, 0)$ while in the corresponding phase of the \mathcal{H} -1 lattice, the \mathbf{Q} -vector varies between approximately $(0.15, 0, 0)$ and $(0.43, 0, 0)$. The majority of the parameter space within the SP_{a-} of both lattices has $\mathbf{Q} = (0.33, 0, 0)$, which are the states shown in Fig. 3. In both lattices, the $\mathbf{Q} = (0.33, 0, 0)$ states are located centrally within the phase and border the $J = 0$ line. The longer \mathbf{Q} -vectors are found in a narrow region bordering the FM_a phase while the shorter \mathbf{Q} -vectors occupy a small region towards the AF Kitaev point.

In the SP_{b+} of the hyperhoneycomb lattice, the \mathbf{Q} -vector

ranges approximately from $(0, 0.17, 0)$ to $(0, 0.40, 0)$ while for the corresponding phase in the \mathcal{H} -1 lattice, the \mathbf{Q} -vector range is smaller: approximately $(0, 0.30, 0)$ to $(0, 0.36, 0)$. For this phase in both lattices, the majority of the parameter space possesses the \mathbf{Q} -vector $(0, 0.33, 0)$ and these are the states shown in Fig. 4. The $(0, 0.33, 0)$ states are located centrally within the phase. The longer \mathbf{Q} -vectors are localized near the FM Kitaev point, while the shorter \mathbf{Q} -vectors border the $SS_{x/y}$ phase.

MQ_1 : In quadrant III of the phase diagram where both Heisenberg and Kitaev exchanges are ferromagnetic, there are two multiple- \mathbf{Q} states that cannot be expressed as a single- \mathbf{Q} ansatz given by Eq. 3. The first of which is a non-coplanar state near the FM Kitaev point and borders both the FM_a and SP_{b+} phases. It has significant Fourier components in $\mathbf{Q} = (0.5, 0.5, x)$ for multiple values of x and does not have a finite net moment.

MQ_2 : The second of the two multiple- \mathbf{Q} states lies closer to the pure- Γ point than the first multiple- \mathbf{Q} state. It also borders both the FM_a and the SP_{b+} phases and is a non-coplanar state. This phase has significant Fourier components in $\mathbf{Q} = (\pm 0.33, \pm 0.33, 0)$, $(\pm 0.33, 0, 0)$, as well as $(0, 0, 0)$, the last of which indicates that it possesses a finite net moment, which lies in the \hat{a} direction. A more detailed analysis of these multiple- \mathbf{Q} states described here are left for future study.

$AF\text{-}SZ_{AF}$: Bordering the AF_c phase is this coplanar phase with vanishing net moment, which is composed of antiferromagnetic chains along the skew-zigzag directions. In the case of the hyperhoneycomb lattice, this phase can be verified via LTA as the exact ground state. This phase is connected to the AF Kitaev point and also partially borders the SP_{a+} phase. In both lattices, the projections of the spins along the \hat{c} direction vanishes. In the hyperhoneycomb lattice, the AF chains along the skew-zigzag directions are collinear and are nearly parallel to the honeycomb-plane of the skew-zigzag. The angle of deviation between the collinear spins and the honeycomb-plane increases as one moves away from the AF_c phase. This trend can be captured by the magnitude of the projection of the spins in the \hat{a} , which is depicted as colour contours in Fig. 2: the larger the projection along \hat{a} , the darker the color. In the \mathcal{H} -1 lattice, the spins along the skew-zigzag directions are not perfectly collinear, but nevertheless the magnitude of the spin projections in the \hat{a} direction also follows the same trend. Furthermore, the non-bridging- z -bonds are antiferromagnetically correlated. In both lattices, the phase preserves the C_2^a rotation symmetry.

$FM\text{-}SZ_{AF}$: This coplanar phase only exists in the \mathcal{H} -1 lattice and is the version of the $AF\text{-}SZ_{AF}$ phase with a finite net moment. This phase is bordered by the SP_{a-} , SP_{a+} , and $AF\text{-}SZ_{AF}$ phases in the AF-Heisenberg regime and is connected to both the AF Kitaev and pure- Γ points. Like the $AF\text{-}SZ_{AF}$ phase of the \mathcal{H} -1 lattice, spins have vanishing projections along the \hat{c} direction, they form near-collinear AF chains along the zigzag directions, and the C_2^a rotation symmetry is preserved. These AF chains become progressively less collinear as one approaches the $J = 0$ line.

Unlike the $AF\text{-}SZ_{AF}$ phase, however, the non-bridging- z -

bonds are ferromagnetically correlated. As a result, despite being in the AF-Heisenberg regime, there is a net moment in the \hat{a} direction. The size of the net moment is small, especially compared to the FM_a phase, and decreases as we approach the SP_{a+} phase or the AF Kitaev point. We illustrate this decrease in net moment by the lightening of the color contours.

B. Existing magnetic orders

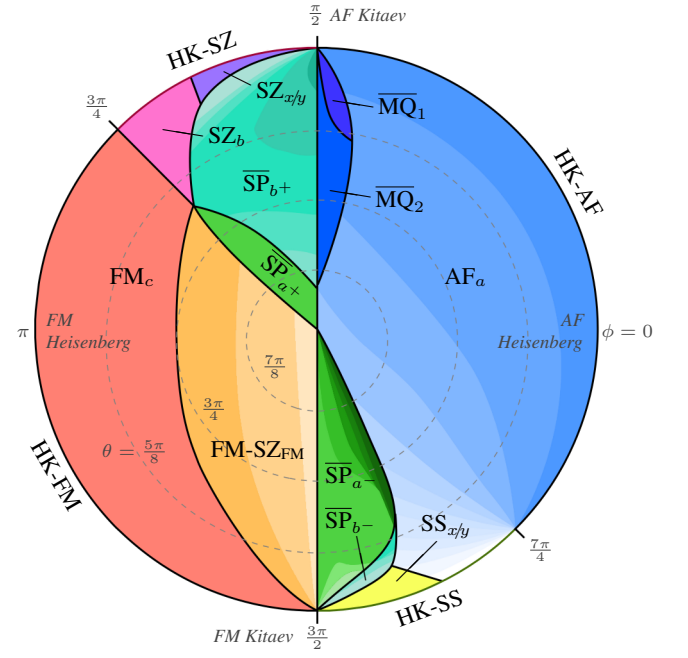
AF_c : This collinear phase is the exact ground state in the AF-Heisenberg region when $J > -K$ and $J > \Gamma$: the LTA succeeds in finding this exact ground state for both lattices. This phase is the HK-AF state with moments aligned antiferromagnetically and locked in the \hat{c} direction due to the presence of Γ .

FM_a : This coplanar state with finite net moment encompasses a large fraction of both phase diagrams. Only in the hyperhoneycomb does the LTA succeed in identifying this phase as the exact ground state. In both lattices, the projection of the spins along the \hat{a} direction is ferromagnetic while the projection along the \hat{c} direction vanishes. The projection along the \hat{b} direction behaves differently for the hyperhoneycomb and the \mathcal{H} -1 models. In the hyperhoneycomb lattice, the \hat{b} component orders in the skew-zigzag order, while in the \mathcal{H} -1 lattice, the \hat{b} component is ferromagnetic within each honeycomb strip. This state is connected to the HK-FM phase, and in the case of the hyperhoneycomb lattice, it is also connected to the $J > -K/2$ segment of the HK-SZ phase, where ObD studies have shown that the HK-SZ phase orders in the \hat{b} direction, much like the FM_a phase. The C_2^a rotation symmetry is preserved in this phase.

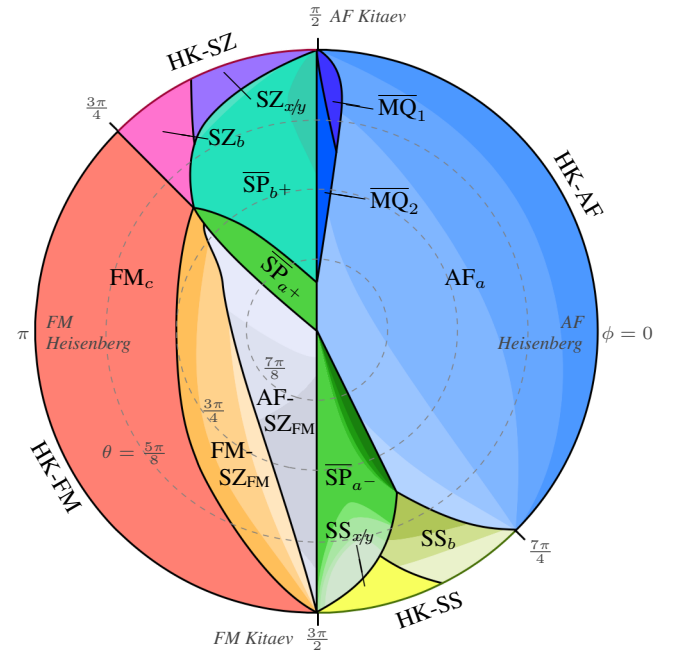
Since the \hat{b} component of the phase in both lattices have a vanishing net moment, only the \hat{a} component contributes to the total moment. This total moment becomes saturated (spins point entirely in the \hat{a} direction) when approaching the HK-FM phase and decreases smoothly as we approach the SP_{a-} boundary. In the hyperhoneycomb case, the total moment further decreases and vanishes smoothly as we approach the HK-SZ phase. The magnitude of the moment along \hat{a} is depicted by the color contours in Fig. 2 where the largest projection is colored darkest.

$\text{SS}_{x/y}$: Wedged within the HK-SS, AF_c , and SP_{b+} phases are two skew-stripy phases, the first of which to be discussed is the non-coplanar $\text{SS}_{x/y}$ phase. This phase has the largest projection along the $x(y)$ direction and this component orders in a skew-stripy fashion (these two orientations are degenerate). In the hyperhoneycomb lattice, the other two Cartesian components of the spins are small but finite and ensure that the spins along each zigzag chain are collinear. In the \mathcal{H} -1 lattice, the $y(x)$ component also orders in a skew-stripy fashion. This phase does not have a net moment and breaks all C_2 symmetries.

SS_b : This other skew-stripy phase is coplanar and lies farther away from the FM Kitaev point relative to the $\text{SS}_{x/y}$ phase. This phase borders the AF_c phase and can be identified via the LTA in the hyperhoneycomb lattice. In both lattices,



(a) Hyperhoneycomb model



(b) \mathcal{H} -1 model

FIG. 5. (Color online) Classical phase diagrams for the J - K - Γ pseudospin model with $\Gamma \leq 0$. The details of this phase diagram can be understood via a classical mapping that relates $(J, K, \Gamma) \rightarrow (-J, -K, -\Gamma)$; see Sec. V C for details. The color contours are guides for the eye: in the case of spiral (SP) states, they represent the length of the \mathbf{Q} -vector, whereas in the case of non-spiral states, they represent properties relevant to that particular phase; see Sec. V for details.

the projection of the spins along the \hat{b} direction orders in a skew-stripy pattern while the \hat{c} projection vanishes. In the hyperhoneycomb lattice, the \hat{a} projection orders antiferromagnetically, while in the \mathcal{H} -1 lattice, spins order ferromagnetically along non-bridging- z -bonds while spins along zigzag chains order antiferromagnetically. This state has a vanishing net moment and preserves the C_2^b rotation symmetry.

SZ_{xy}: Analogous to the SS_{*x/y*} phase, there exists a non-coplanar, skew-zigzag phase with a vanishing net moment near the AF Kitaev point bordering the SP_{*a*-} phase that breaks all C_2 symmetries. This phase has the largest projection along the $x(y)$ direction and this component orders in a skew-zigzag pattern (these two configurations are degenerate). In the hyperhoneycomb lattice, the other two Cartesian spin components ensure that the spins are collinear along zigzag chains. In the \mathcal{H} -1 lattice, the $y(x)$ component is also ordered in the skew-zigzag pattern. This phase is closely related to the SZ_{*x/y*} phase: these two phases map onto each other under the $(J, K, \Gamma) \rightarrow (-J, -K, -\Gamma)$ classical transformation.

SZ_{*b*}: In the \mathcal{H} -1 model, an additional coplanar, skew-zigzag phase with vanishing net moment exists. This phase borders the FM_{*a*}, SZ_{*x/y*}, SP_{*a*-}, and HK-SZ phases. It forms ferromagnetic skew-zigzag chains with antiferromagnetic non-bridging- z bonds and preserves the C_2^a rotation symmetry. The component along \hat{c} vanishes while the projection along \hat{b} is the greatest. This phase is closely related to the SS_{*b*} phase: these two phases map onto each other under the $(J, K, \Gamma) \rightarrow (-J, -K, -\Gamma)$ classical transformation.

C. Phase diagrams for $\Gamma \leq 0$ and connection to experimental results

As mentioned previously, the classical transformation of applying time-reversal on the odd sublattices maps $(J, K, \Gamma) \rightarrow (-J, -K, -\Gamma)$. Using this transformation, the classical phase diagrams for $\Gamma \geq 0$ in Fig. 2 can be inverted to yield the phase diagrams for $\Gamma \leq 0$ in Fig. 5, where the radial coordinate now maps to $r = \theta \in [\pi, \frac{\pi}{2}]$. Under this transformation, ferromagnetic components become antiferromagnetic, while stripy components become zig-zag (these transformed phases are labeled in Fig. 5). For the spiral and multiple- \mathbf{Q} states, we use an overhead bar (i.e. $\overline{\text{SP}}_{a-}$ versus SP_{*a*-}) to emphasize the close relationship between the $\Gamma \leq 0$ and the $\Gamma \geq 0$ phases. For the spiral phases, we note that the \mathbf{Q} -vector range remains invariant after this transformation, while the C_2 rotation that the spiral state was invariant under must now be followed by a time-reversal operation Θ .

We draw special attention to the $\overline{\text{SP}}_{a-}$ phases found in the $\Gamma \leq 0$ region because of their close relationship to the experimental magnetic orders (the real-space configuration of these spiral phases can be seen in Fig. 6 and can be directly compared with those found in Refs. 47 and 48).

The experimental magnetic ordering of the hyperhoneycomb Li₂IrO₃⁴⁸ possesses the same symmetries as that of SP_{*a*-}: following the analysis used in Ref. 48, we discern that the SP_{*a*-} phase on the hyperhoneycomb lattice is described by the magnetic basis vector combination (iA_a, iC_b, F_c) ⁶⁸,

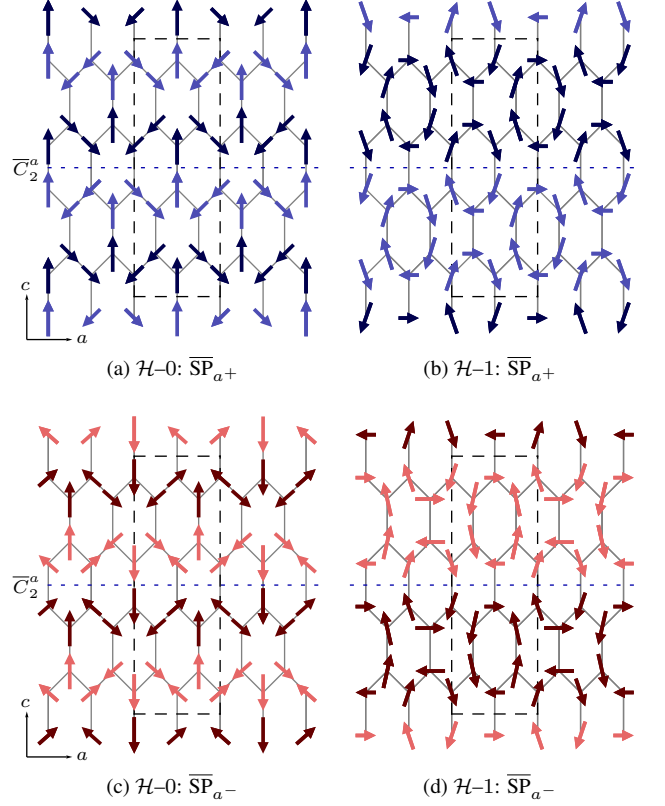


FIG. 6. (Color online) Real-space spin configurations of the $\overline{\text{SP}}_a$ spiral states obtained from simulated annealing with spins projected on to the ac -plane. The chosen parameter points yield $\mathbf{Q} = (0.33, 0, 0)$; however, we note that the \mathbf{Q} -vector in these phases are generally incommensurate and are not the same as the peak positions of the structure factor (see main text and Figs. 11, 12). The black dashed box enclose the conventional unit cell. Identical colors indicate that the sublattices share spiral-planes. Shades of blue indicate that the spiral-planes are aligned with the honeycomb-planes while shades of red indicate that the spiral-planes are not aligned with the honeycomb-planes. The handedness of adjacent sites can be readily verified as being opposite: the spirals counter-propagate. Examples of the preserved rotation followed by time-reversal operation ($\overline{C}_2^a = \Theta \cdot C_2^a$ where Θ is the time-reversal operation) are indicated by the dotted blue lines.

which is identical to that of the experimental magnetic ordering⁴⁸, indicating that these two phases are indeed the same. In addition, the experimental ordering wavevector— $\mathbf{Q}_{\text{exp}} = (0.57, 0, 0)$ —lies within the range found in our model (when expressed using the same definition as \mathbf{Q}_{exp} from Ref. 48, the wavevectors found within our present model is $(h'00)$ where $0.53 \lesssim h' \lesssim 0.80$).

For the \mathcal{H} -1 Li₂IrO₃⁴⁷, \mathbf{Q}_{exp} also lies within the range found in our model. Using the notation defined in Ref. 47, the magnetic basis vector combination that describes the $\overline{\text{SP}}_{a-}$ phase is $[i(A, -A)_a, -i(C, -C)_b, (F, F)_c]$, which only differs from the experimental combination of $[i(A, -A)_a, (-1)^m i(F, -F)_b, (F, F)_c]$ in the S_b -component.

For completeness, we also show the real-space configurations of the SP_{*a*+} and SP_{*b*} phases in Figs. 6 and 7 respectively,

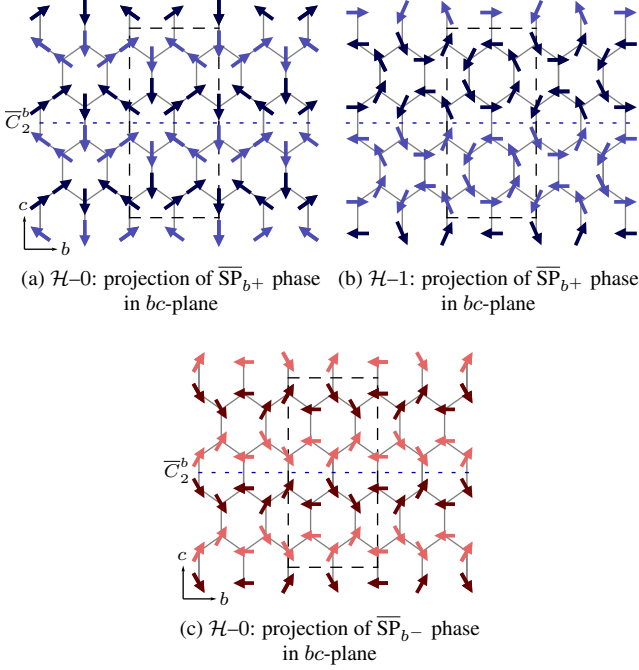


FIG. 7. (Color online) Real-space spin configurations of the $\overline{\text{SP}}_b$ spiral states obtained from simulated annealing with spins projected on to the bc -plane. The chosen parameter points yield $\mathbf{Q} = (0, 0.33, 0)$; however, we note that the \mathbf{Q} -vector in these phases are generally incommensurate. See caption in Fig. 6 for further details. $\overline{C}_2^b = \Theta \cdot C_2^b$ where Θ is the time-reversal operation. In the case of the $\overline{\text{SP}}_b-$ phase, only the spiral planes and not the spins preserve the \overline{C}_2^b operation.

as a comparison with Figs. 3 and 4. Magnetic static structure factors of these spiral phases can be found in Appendix C.

VI. DISCUSSION AND OUTLOOK

In the model presented, we have implicitly assumed an ideal crystal structure. In principle, distortions of the oxygen octahedra as well as Ir positions can bring about additional anisotropic exchange interactions between neighboring pseudospins.^{41,42} In addition, large distortions can admix the $j_{\text{eff}} = 1/2$ and the neglected orbitals, which can generate anisotropic g -factors or even destroy the $j_{\text{eff}} = 1/2$ description entirely.²⁰ Nevertheless, these distortion effects are likely to be smaller in the 3D compounds compared to the 2D honeycomb iridates, since the octahedral environments in the former are more ideal than those of the latter.^{7,45,46,69} As such, these distortion effects may serve only to affect quantitatively the phases found within our treatment while the qualitative features of our phase diagrams can be expected to remain robust.

We have also assumed that the 3D materials lie deep in the Mott insulating regime ($U \rightarrow \infty$) such that other hopping pathways, namely ones involving multiple oxygen and lithium ions, can be neglected, thus resulting in a model with only NN exchanges. The role of further neighbors have been considered in the 2D honeycomb iridates: further neighbor hopping

in *ab initio* treatments^{24,25,27,44}, as well as further neighbor exchanges in the localized picture^{19,43} have been investigated. In addition, experimental work has suggested the possibility of significant further neighbor interactions in the case of the 2D Li_2IrO_3 .⁷⁰ Meanwhile, there have also been studies on effects of further neighbors in the case of the hyperhoneycomb iridate in both the itinerant picture⁴⁹ and in the Mott limit⁵³. The effects of further neighbors have revealed interesting consequences in these cases, which suggests that additional studies on this subject and its role in a minimal model for the hyperhoneycomb and \mathcal{H} -1 lattices may be warranted.

On the other hand, if the ideal NN localized picture is adequate in capturing the magnetic order of the whole family of honeycomb iridates, then we may expect the 2D honeycomb, hyperhoneycomb, and \mathcal{H} -1 iridates to be describable by NN J - K - Γ models. The 2D- Li_2IrO_3 and the two 3D- Li_2IrO_3 are then expected to have comparable exchange parameters, since their chemical composition and local crystal structures are similar, while the 2D- Na_2IrO_3 is more distorted and may lie in a different region in parameter space. Since the 2D- Na_2IrO_3 orders in a zigzag fashion^{5,7,21} and the 2D- Li_2IrO_3 is believed to order in a spiral phase^{43,71}, this line of reasoning suggests that the 3D- Li_2IrO_3 's may order in one of the spiral phases, especially since the spiral regions are relatively larger and the zigzag region smaller in the 3D phase diagrams. Indeed, the two 3D- Li_2IrO_3 have been experimentally reported to order in a non-collinear fashion, with counter-propagating spirals^{47,48}. The ordering pattern in the case of the hyperhoneycomb Li_2IrO_3 case is precisely that of the hyperhoneycomb $\overline{\text{SP}}_{a-}$ phase⁴⁸, while that of the \mathcal{H} -1 Li_2IrO_3 has striking similarities with the \mathcal{H} -1 $\overline{\text{SP}}_{a-}$ phase⁴⁷. Moreover, the similar thermodynamic properties of the two 3D- Li_2IrO_3 lattices may be due to the combination of the near-identical phase diagrams and the fact that both systems are near ideal (distortion-free) and largely driven by NN physics.

In summary, motivated by the similar behaviors and local structure of the hyperhoneycomb and \mathcal{H} -1 Li_2IrO_3 , we studied the NN pseudospin J - K - Γ model, which contains the Heisenberg, the Kitaev, and the off-diagonal Γ exchange interactions. We argue that with strong on-site interaction and atomic spin-orbit coupling, these models are minimal effective models for the $j_{\text{eff}} = 1/2$ pseudospins in these 3D honeycomb-based materials. The resulting classical phase diagrams that emerge in the two cases are very similar. On the other hand, when compared with the phase diagram of the 2D honeycomb lattice, the zigzag region diminished while spiral phases with counter-propagating spirals expanded in the 3D phase diagrams. We characterized all the magnetic orders in detail and provided static structure factor results of the spiral phases. We believe that our phase diagrams and detailed analysis will be relevant in identifying the phases of the 3D- Li_2IrO_3 compounds, and our model can serve as the minimal starting point in identifying the common thread which runs through this family of iridium-based materials.

TABLE I. Summary of magnetic phases for $\Gamma \geq 0$. For detailed description of each phase, see Sec. V. Magnetic phases for $\Gamma \leq 0$ are obtained by acting the time-reversal operation on odd sublattices on the phases summarized here; see Sec. VC for details. Under this classical transformation, the \mathbf{Q} -vector range of the spiral phases remain invariant, while the preserved C_2 symmetry must now be followed by the time-reversal operation Θ , *e.g.* the transformed spiral states SP_{a+} are invariant under $\bar{C}_2^a \equiv \Theta \cdot C_2^a$.

	S_{tot}^a	$\mathcal{H}-0^b$	$\mathcal{H}-1^b$	Collinear/ coplanar	Preserved symmetry	Structure factor peak (\mathbf{q}) ^c	\mathbf{Q} -vector range ^d	Notes
SP_{a+}		NM	NM		C_2^a	$(\mathbf{1}_a + \mathbf{Q})$	$\sim (0.33, 0, 0)$	spiral-planes aligned with honeycomb-planes
SP_{b+}		NM	NM		C_2^b	$(\mathbf{1}_b + \mathbf{Q})$	$(0k0)$ $\mathcal{H}-0: 0.17 \lesssim k \lesssim 0.40$ $\mathcal{H}-1: 0.30 \lesssim k \lesssim 0.36$	spiral-planes aligned with honeycomb-planes
SP_{a-}		NM	NM		C_2^a	$(\mathbf{1}_a - \mathbf{Q})$	$(h00)$ $\mathcal{H}-0: 0.20 \lesssim h \lesssim 0.47$ $\mathcal{H}-1: 0.15 \lesssim h \lesssim 0.43$	spiral-planes not aligned with honeycomb-planes
SP_{b-}		NM	n/a		C_2^{be}	$(\mathbf{1}_b - \mathbf{Q})$	$\sim (0, 0.33, 0)$	spiral-planes not aligned with honeycomb-planes
MQ_1		NM	NM				$(0.5, 0.5, x)$	multiple- q state
MQ_2	\hat{a}	NM	NM				$(\pm 0.33, \pm 0.33, 0),$ $(\pm 0.33, 0, 0), (0, 0, 0)$	multiple- \mathbf{Q} state with finite moment
AF-SZ_{AF}		LTA	NM	copl.	C_2^a			AF skew-zigzag chains
FM-SZ_{AF}	\hat{a}	n/a	NM	copl.	C_2^a			AF skew-zigzag chains, FM non-bridging- z -bonds
AF_c		LTA	LTA	col.	$C_2^a/C_2^b/C_2^c$			AF order along \hat{c}
FM_a	\hat{a}	LTA	NM	copl.	C_2^a			$S_i \cdot \hat{a}$: FM order
SS_b		LTA	NM	copl.	C_2^b			$S_i \cdot \hat{b}$: SS order
SZ_b		n/a	NM	copl.	C_2^b			$S_i \cdot \hat{b}$: SZ order
$\text{SS}_{x/y}$		NM	NM					$S_i \cdot \hat{x}$ or $S_i \cdot \hat{y}$: SS order (degenerate)
$\text{SZ}_{x/y}$		NM	NM					$S_i \cdot \hat{x}$ or $S_i \cdot \hat{y}$: SZ order (degenerate)

^a Indicates the direction of the total moment, if finite

^b Method that the ground state was determined: Luttinger-Tisza approximation (LTA) or numerical minimization via single- \mathbf{Q} ansatz and simulated annealing (NM); a blank entry is assigned if the phase does not exist for the given model

^c $\mathbf{1}_a = (100)$ and $\mathbf{1}_b = (010)$.

^d Using the alternative definition of the ordering wavevector in Refs. 47 and 48 (hereby denoted as \mathbf{Q}'), the spiral phases considered in this work are characterized by $\mathbf{Q}' = (\mathbf{1}_x - \mathbf{Q})$, *i.e.* for the SP_{a-} phase of the hyperhoneycomb lattice, $\mathbf{Q}' = (h'00)$ where $0.53 \lesssim h' \lesssim 0.80$.

^e Only the spiral-planes and not the spins preserve the rotation symmetry

ACKNOWLEDGMENTS

We thank R. Schaffer and J. Rau for discussions. We also thank R. Coldea for his useful comments on our work and for making some of the results in Refs. 47 and 48 available prior to publication. Computations were performed on the GPC supercomputer at the SciNet HPC Consortium. SciNet is funded by: the Canada Foundation for Innovation under the auspices of Compute Canada; the Government of Ontario; Ontario Research Fund - Research Excellence; and the University of Toronto. This research was supported by the NSERC, CIFAR, and Centre for Quantum Materials at the University of Toronto.

Upon initial submission of this manuscript to the preprint arXiv, independent experimental results on the magnetic structure of $\mathcal{H}-1$ Li_2IrO_3 were released⁴⁷ which reported the existence of a spiral order in the compound. In addition, independent experimental report of the existence of a spiral order

in hyperhoneycomb Li_2IrO_3 was released⁴⁸ after the submission of this work. Although this work is an exploratory study of our pseudospin model, we have since made modifications to reference these experimental results throughout the current manuscript wherever relevant.

Appendix A: Details on the strong-coupling expansion

Octahedral crystal fields arising from the oxygen ions split the Ir^{4+} $5d$ orbitals into the lower energy t_{2g} and higher energy e_g multiplets. Large atomic spin-orbit coupling further split the t_{2g} orbitals into the lowest energy $j_{\text{eff}} = 3/2$ quadruplet and higher energy $j_{\text{eff}} = 1/2$ doublets. The five electrons at each Ir^{4+} site fully-fill the $j_{\text{eff}} = 3/2$ orbitals and half-fill the $j_{\text{eff}} = 1/2$ orbitals, leaving the e_g orbitals unoccupied. In the limit of large atomic spin-orbit coupling and strong on-site electron correlations, the $j_{\text{eff}} = 3/2$ and e_g orbitals can be projected out and the relevant low-energy degrees of freedom

are the localized $j_{\text{eff}} = 1/2$ pseudospins.

In the presence of hopping between neighboring Ir orbitals, the perturbed ground states can be captured by an effective Hamiltonian derived by a strong coupling expansion. We assume the unperturbed, atomic Hamiltonian to be comprised of atomic SOC and on-site interactions. The atomic SOC takes the form $H_{\text{SOC}} = -\sum_a \lambda_a \cdot s_a$, where s_a and l_i are the spin and effective t_{2g} orbital angular momentum of electron a . The on-site interaction consists of Hund's coupling and intra/inter-orbital repulsion, which we write in the Kanamori form

$$H_{\text{on-site}} = \sum_i \left[\frac{U - 3J_H}{2} (N_i - 5)^2 - 2J_H S_i^2 - \frac{J_H}{2} L_i^2 \right] \quad (\text{A1})$$

where N_i , S_i , and L_i are the total number, spin, and effective orbital angular momentum at site i ; U and J_H are the Coulomb repulsion and Hund's coupling respectively. The perturbation comes in the form of NN hopping amplitudes between t_{2g} orbitals: we introduce both direct orbital overlaps and effective hopping between neighboring orbitals mediated by the edge-shared oxygens. The hopping amplitudes can be written as

$$H_{\text{hop}} = \sum_{\langle i,j \rangle \in \alpha\beta(\gamma)} \left[t_1 \left(d_{i\alpha}^\dagger d_{j\alpha} + d_{i\beta}^\dagger d_{j\beta} \right) + t_2 \left(d_{i\alpha}^\dagger d_{j\beta} + d_{i\beta}^\dagger d_{j\alpha} \right) + t_3 d_{i\gamma}^\dagger d_{j\gamma} \right], \quad (\text{A2})$$

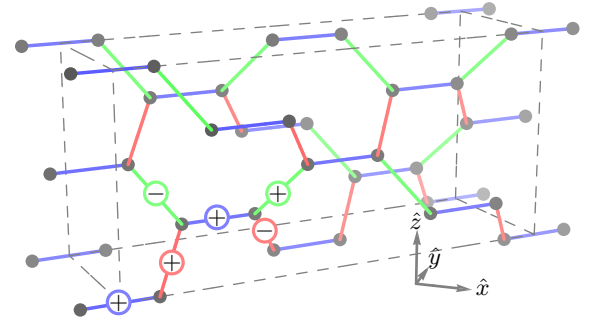
where $\gamma \in (x, y, z)$ is the label for bond $\langle i, j \rangle$, and α, β are the other two components. The creation operator is given by $d_{i\alpha}^\dagger = (d_{i\alpha\uparrow}^\dagger, d_{i\alpha\downarrow}^\dagger)$ and creates electrons on site i in orbital α , where the t_{2g} orbitals are labeled according to $x \rightarrow yz$, $y \rightarrow xz$, and $z \rightarrow xy$. The hopping amplitudes are given by

$$t_1 = \frac{t_{dd\pi} + t_{dd\delta}}{2}, t_2 = \frac{t_{pd\pi}^2}{\Delta} + \frac{t_{dd\pi} - t_{dd\delta}}{2}, t_3 = \frac{3t_{dd\sigma} + t_{dd\delta}}{4} \quad (\text{A3})$$

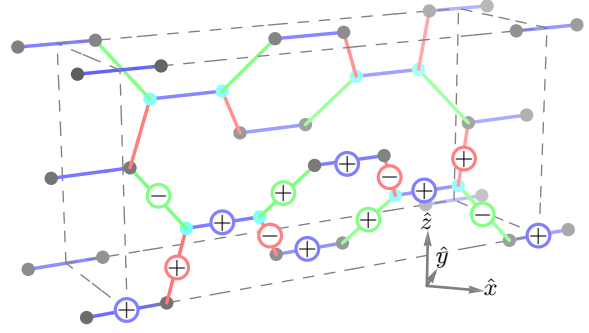
where $t_{dd\sigma}$, $t_{dd\pi}$, $t_{dd\delta}$, and $t_{pd\pi}$ are the Slater-Koster amplitudes parametrizing direct Ir orbital overlaps and O-Ir orbital overlaps respectively, while Δ is the energy gap between oxygen and iridium.

In the large SOC limit, we perform the strong coupling expansion with the limit $U > \lambda \gg J_H \gg t$ then project into the $j_{\text{eff}} = 1/2$ manifold. The resulting $j_{\text{eff}} = 1/2$ pseudospin Hamiltonian then takes the form of Eq. 1 with exchanges related to hopping amplitudes by Eq. 2. For more detail on the derivation of the expansion, we refer the reader to the appendix in Ref. 40.

From Eq. 2, we note that the exchanges depend sensitively on the relative signs and magnitudes of the hopping amplitudes t_{1-3} . Hence, a detailed analysis of the underlying band structure would greatly aid the realistic estimations of these exchanges for the 3D Li_2IrO_3 systems.



(a) Hyperhoneycomb lattice



(b) \mathcal{H} -1 lattice

FIG. 8. (Color online) Relative signs of Γ chosen for the hyperhoneycomb and \mathcal{H} -1 lattices. The plus/minus sign on each bond corresponds to the sign in front of Γ that appears in the Hamiltonian in Eq. 1. With this choice of relative signs in Γ , we are still free to choose either a positive or a negative value for Γ . The x , y , and z bonds are colored red, green, and blue, respectively. The bridging-sites are colored cyan. The gray dashed boxes are the conventional unit cells.

Appendix B: Sign structure of Γ

Although the relative signs of Γ among symmetry-equivalent bonds can be determined by applying the appropriate symmetry transformation, the relative signs among symmetry-inequivalent bonds are not constrained by crystal symmetries. However, these symmetry-inequivalent bonds have identical local environments (e.g. nearest-neighbor oxygen and cation hopping pathways), and hence, the sign structure of Γ among symmetry-inequivalent bonds are expected to follow transformations that preserve these local environments. For example, to relate the signs of Γ on the x - and z -bonds emanating from a site, a C_2 rotation through the site and along the connecting y -bond would preserve the local oxygen and cation environments while mapping the x -bond to the z -bond. This microscopic justification of the relative signs of Γ was used in assigning the sign structures in Fig. 8. We emphasize that this convention only fixes the *relative* signs Γ in the lattice: Γ can still be either positive or negative, leading to the phase diagrams in Figs. 2 and 5 respectively. We leave

other possible choices of relative signs in Γ among symmetry-inequivalent bonds for future study.

Appendix C: Magnetic structure factors

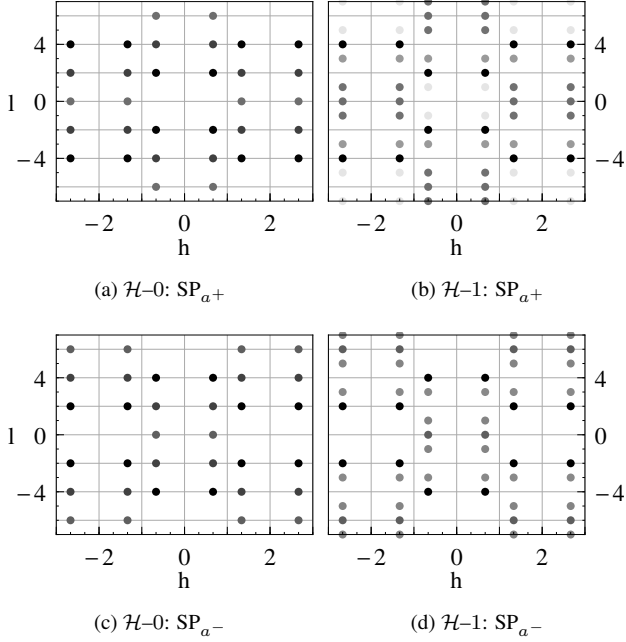


FIG. 9. Static structure factors along the $(h0l)$ plane for the SP_a phases presented in Fig. 3. These states are characterized by $\mathbf{Q} = (0.33, 0, 0)$. The darkness of the dots indicate the peaks' relative intensities. The + spiral phases have peaks at $\mathbf{q} = (\mathbf{1}_a + \mathbf{Q}) = (1.33, 0, 0)$ while the - spiral phases have peaks at $\mathbf{q} = (\mathbf{1}_a - \mathbf{Q}) = (0.66, 0, 0)$, where $\mathbf{1}_a = (100)$.

The magnetic static structure factors along certain momentum cuts of the SP_a , SP_b , \overline{SP}_a , and \overline{SP}_b phases of both the hyperhoneycomb and \mathcal{H} -1 lattices are presented in Figs. 9, 10, 11, and 12 respectively for reference.

- ¹ D. Yanagishima and Y. Maeno, *Journal of the Physical Society of Japan* **70**, 2880 (2001).
- ² S. Nakatsuji, Y. Machida, Y. Maeno, T. Tayama, T. Sakakibara, J. van Duijn, L. Balicas, J. N. Millican, R. T. Macaluso, and J. Y. Chan, *Physical Review Letters* **96**, 087204 (2006).
- ³ K. Matsuhira, M. Wakeshima, R. Nakanishi, T. Yamada, A. Nakamura, W. Kawano, S. Takagi, and Y. Hinatsu, *Journal of the Physical Society of Japan* **76**, 3706 (2007).
- ⁴ Y. Singh and P. Gegenwart, *Phys. Rev. B* **82**, 064412 (2010).
- ⁵ X. Liu, T. Berlijn, W.-G. Yin, W. Ku, A. Tsvelik, Y.-J. Kim, H. Gretarsson, Y. Singh, P. Gegenwart, and J. P. Hill, *Phys. Rev. B* **83**, 220403 (2011).
- ⁶ Y. Singh, S. Manni, J. Reuther, T. Berlijn, R. Thomale, W. Ku, S. Trebst, and P. Gegenwart, *Phys. Rev. Lett.* **108**, 127203 (2012).
- ⁷ S. K. Choi, R. Coldea, A. N. Kolmogorov, T. Lancaster, I. I. Mazin, S. J. Blundell, P. G. Radaelli, Y. Singh, P. Gegenwart, K. R. Choi, S.-W. Cheong, P. J. Baker, C. Stock, and J. Taylor, *Phys. Rev. Lett.* **108**, 127204 (2012).
- ⁸ T. Qi, O. Korneta, X. Wan, L. DeLong, P. Schlottmann, and G. Cao, *Journal of Physics: Condensed Matter* **24**, 345601 (2012).
- ⁹ M. Z. Hasan and C. L. Kane, *Rev. Mod. Phys.* **82**, 3045 (2010).

- ¹⁰ X.-L. Qi and S.-C. Zhang, *Rev. Mod. Phys.* **83**, 1057 (2011).
- ¹¹ M. Z. Hasan and J. E. Moore, *Ann. Rev. Cond. Mat. Phys.* **2**, 55 (2011).
- ¹² D. Pesin and L. Balents, *Nature Physics* **6**, 376 (2010).
- ¹³ B.-J. Yang and Y. B. Kim, *Physical Review B* **82**, 085111 (2010).
- ¹⁴ Y.-Z. You, I. Kimchi, and A. Vishwanath, *Phys. Rev. B* **86**, 085145 (2012).
- ¹⁵ W. Witczak-Krempa, G. Chen, Y.-B. Kim, and L. Balents, *Condensed Matter Physics* **5**, 2014 (2013).
- ¹⁶ G. Jackeli and G. Khaliullin, *Phys. Rev. Lett.* **102**, 017205 (2009).
- ¹⁷ A. Shitade, H. Katsura, J. Kuneš, X.-L. Qi, S.-C. Zhang, and N. Nagaosa, *Phys. Rev. Lett.* **102**, 256403 (2009).
- ¹⁸ J. c. v. Chaloupka, G. Jackeli, and G. Khaliullin, *Phys. Rev. Lett.* **105**, 027204 (2010).
- ¹⁹ I. Kimchi and Y.-Z. You, *Phys. Rev. B* **84**, 180407 (2011).
- ²⁰ S. Bhattacharjee, S.-S. Lee, and Y. B. Kim, *New Journal of Physics* **14**, 073015 (2012).
- ²¹ F. Ye, S. Chi, H. Cao, B. C. Chakoumakos, J. A. Fernandez-Baca, R. Custelcean, T. F. Qi, O. B. Korneta, and G. Cao, *Phys. Rev. B* **85**, 180403 (2012).
- ²² S. Lovesey and A. Dobrynin, *Journal of Physics: Condensed Mat-*

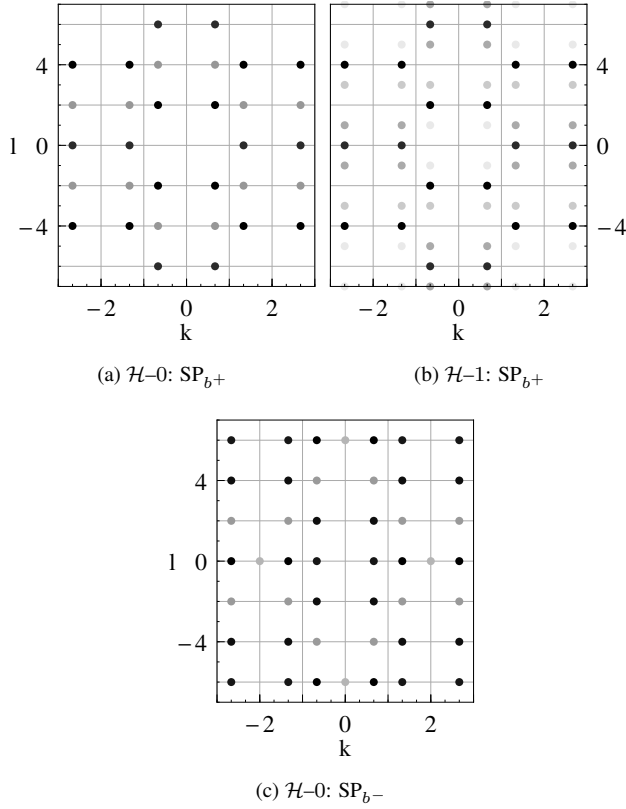


FIG. 10. Static structure factors along the $(0kl)$ plane for the SP_b phases presented in Fig. 4. These states are characterized by $\mathbf{Q} = (0, 0.33, 0)$. The darkness of the dots indicate the peaks' relative intensities. The $+$ spiral phases have peaks at $\mathbf{q} = (\mathbf{1}_b + \mathbf{Q}) = (0, 1.33, 0)$ while the $-$ spiral phase has a peak at $\mathbf{q} = (\mathbf{1}_b - \mathbf{Q}) = (0, 0.66, 0)$, where $\mathbf{1}_b = (010)$.

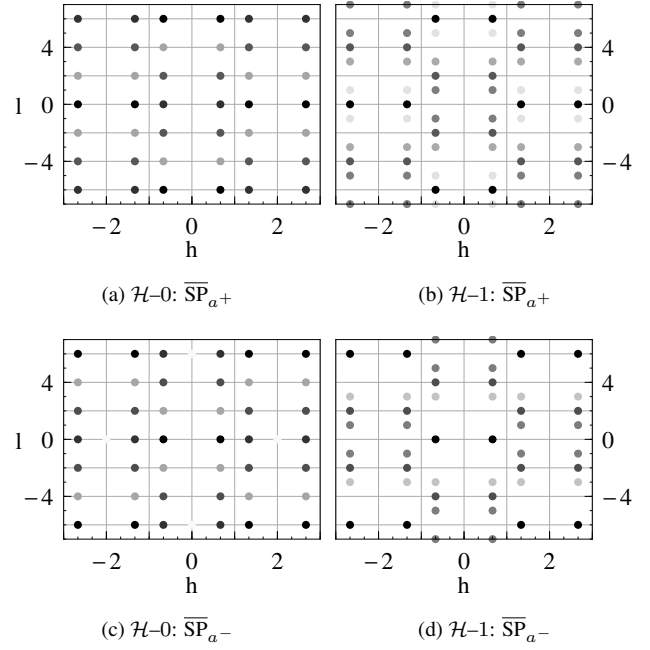


FIG. 11. Static structure factors along the $(h0l)$ plane for the $\Gamma \leq 0$ SP_a phases presented in Fig. 6. These states are characterized by $\mathbf{Q} = (0.33, 0, 0)$. The darkness of the dots indicate the peaks' relative intensities.

- ter **24**, 382201 (2012).
- ²³ R. Comin, G. Levy, B. Ludbrook, Z.-H. Zhu, C. N. Veenstra, J. A. Rosen, Y. Singh, P. Gegenwart, D. Stricker, J. N. Hancock, D. van der Marel, I. S. Elfimov, and A. Damascelli, *Phys. Rev. Lett.* **109**, 266406 (2012).
- ²⁴ C. H. Kim, H. S. Kim, H. Jeong, H. Jin, and J. Yu, *Phys. Rev. Lett.* **108**, 106401 (2012).
- ²⁵ I. I. Mazin, H. O. Jeschke, K. Foyevtsova, R. Valentí, and D. I. Khomskii, *Phys. Rev. Lett.* **109**, 197201 (2012).
- ²⁶ R. Schaffer, S. Bhattacharjee, and Y. B. Kim, *Phys. Rev. B* **86**, 224417 (2012).
- ²⁷ K. Foyevtsova, H. O. Jeschke, I. I. Mazin, D. I. Khomskii, and R. Valentí, *Phys. Rev. B* **88**, 035107 (2013).
- ²⁸ J. P. Clancy, N. Chen, C. Y. Kim, W. F. Chen, K. W. Plumb, B. C. Jeon, T. W. Noh, and Y.-J. Kim, *Phys. Rev. B* **86**, 195131 (2012).
- ²⁹ H. Gretarsson, J. P. Clancy, X. Liu, J. P. Hill, E. Bozin, Y. Singh, S. Manni, P. Gegenwart, J. Kim, A. H. Said, D. Casa, T. Gog, M. H. Upton, H.-S. Kim, J. Yu, V. M. Katukuri, L. Hozoi, J. van den Brink, and Y.-J. Kim, *Phys. Rev. Lett.* **110**, 076402 (2013).
- ³⁰ H. Gretarsson, J. P. Clancy, Y. Singh, P. Gegenwart, J. P. Hill, J. Kim, M. H. Upton, A. H. Said, D. Casa, T. Gog, and Y.-J. Kim, *Phys. Rev. B* **87**, 220407 (2013).
- ³¹ J. c. v. Chaloupka, G. Jackeli, and G. Khaliullin, *Phys. Rev. Lett.* **110**, 097204 (2013).
- ³² G. Cao, T. F. Qi, L. Li, J. Terzic, V. S. Cao, S. J. Yuan, M. Tovar, G. Murthy, and R. K. Kaul, *Phys. Rev. B* **88**, 220414 (2013).
- ³³ A. Kitaev, *Annals of Physics* **321**, 2 (2006).
- ³⁴ S. Yang, D. L. Zhou, and C. P. Sun, *Phys. Rev. B* **76**, 180404 (2007).
- ³⁵ H. Yao and S. A. Kivelson, *Phys. Rev. Lett.* **99**, 247203 (2007).
- ³⁶ T. Si and Y. Yu, *Nuclear Physics B* **803**, 428 (2008).
- ³⁷ S. Mandal and N. Surendran, *Phys. Rev. B* **79**, 024426 (2009).
- ³⁸ V. Chua, H. Yao, and G. A. Fiete, *Phys. Rev. B* **83**, 180412 (2011).
- ³⁹ M. Hermanns and S. Trebst, *Phys. Rev. B* **89**, 235102 (2014).
- ⁴⁰ J. G. Rau, E. K.-H. Lee, and H.-Y. Kee, *Phys. Rev. Lett.* **112**, 077204 (2014).
- ⁴¹ V. M. Katukuri, S. Nishimoto, V. Yushankhai, A. Stoyanova, H. Kandpal, S. Choi, R. Coldea, I. Rousochatzakis, L. Hozoi, and J. van den Brink, *New Journal of Physics* **16**, 013056 (2014).
- ⁴² Y. Yamaji, Y. Nomura, M. Kurita, R. Arita, and M. Imada, *arXiv preprint arXiv:1402.1030* (2014).
- ⁴³ J. Reuther, R. Thomale, and S. Rachel, *arXiv preprint arXiv:1404.5818* (2014).
- ⁴⁴ H.-S. Kim, C. H. Kim, H. Jeong, H. Jin, and J. Yu, *Phys. Rev. B* **87**, 165117 (2013).
- ⁴⁵ T. Takayama, A. Kato, R. Dinnebier, J. Nuss, and H. Takagi, *arXiv preprint arXiv:1403.3296* (2014).
- ⁴⁶ K. Modic, T. E. Smidt, I. Kimchi, N. P. Breznay, A. Biffin, S. Choi, R. D. Johnson, R. Coldea, P. Watkins-Curry, G. T. McCandless, *et al.*, *Nature communications* **5** (2014).
- ⁴⁷ A. Biffin, R. Johnson, I. Kimchi, R. Morris, A. Bombardi, J. Analytis, A. Vishwanath, and R. Coldea, *arXiv preprint arXiv:1407.3954* (2014).
- ⁴⁸ A. Biffin, R. Johnson, S. Choi, F. Freund, S. Manni, A. Bombardi, P. Manuel, P. Gegenwart, and R. Coldea, *arXiv preprint arXiv:1408.0246* (2014).
- ⁴⁹ E. K.-H. Lee, S. Bhattacharjee, K. Hwang, H.-S. Kim, H. Jin, and

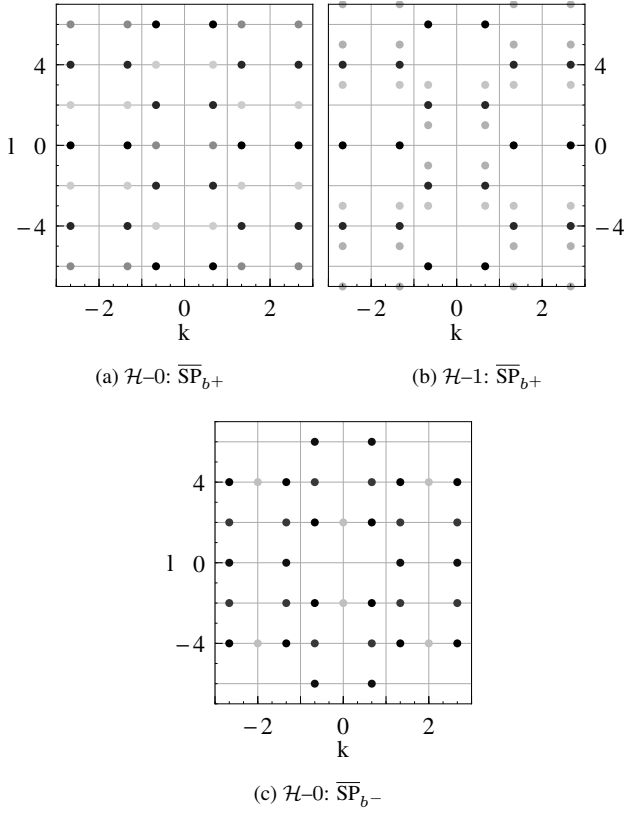


FIG. 12. Static structure factors along the $(0kl)$ plane for the $\Gamma \leq 0$ $\overline{\text{SP}}_b$ phases presented in Fig. 7. These states are characterized by $\mathbf{Q} = (0, 0.33, 0)$. The darkness of the dots indicate the peaks' relative intensities.

- Y. B. Kim, *Phys. Rev. B* **89**, 205132 (2014).
⁵⁰ E. K.-H. Lee, R. Schaffer, S. Bhattacharjee, and Y. B. Kim, *Phys. Rev. B* **89**, 045117 (2014).
⁵¹ S. Lee, E. K.-H. Lee, A. Paramakanti, and Y. B. Kim, *Phys. Rev. B* **89**, 014424 (2014).
⁵² J. Nasu, T. Kaji, K. Matsuura, M. Udagawa, and Y. Motome, *Phys. Rev. B* **89**, 115125 (2014).
⁵³ S. Lee, J.-S. Jeong, K. Hwang, and Y. B. Kim, *arXiv preprint*

- arXiv:1403.2724* (2014).
⁵⁴ I. Kimchi, J. G. Analytis, and A. Vishwanath, *arXiv preprint* *arXiv:1309.1171* (2013).
⁵⁵ J. Nasu, M. Udagawa, and Y. Motome, *arXiv preprint* *arXiv:1406.5415* (2014).
⁵⁶ B. Kim, H. Jin, S. Moon, J.-Y. Kim, B.-G. Park, C. Leem, J. Yu, T. Noh, C. Kim, S.-J. Oh, *et al.*, *Physical Review Letters* **101**, 076402 (2008).
⁵⁷ Z. Nussinov and J. v. d. Brink, *arXiv preprint* *arXiv:1303.5922* (2013).
⁵⁸ J. C. Slater and G. F. Koster, *Phys. Rev.* **94**, 1498 (1954).
⁵⁹ S. Okamoto, *Phys. Rev. B* **87**, 064508 (2013).
⁶⁰ J. M. Luttinger and L. Tisza, *Phys. Rev.* **70**, 954 (1946).
⁶¹ D. Litvin, *Physica* **77**, 205 (1974).
⁶² J. Reuther, R. Thomale, and S. Trebst, *Phys. Rev. B* **84**, 100406 (2011).
⁶³ C. Price and N. B. Perkins, *Phys. Rev. B* **88**, 024410 (2013).
⁶⁴ G. Khaliullin, *Progress of Theoretical Physics Supplement* **160**, 155 (2005).
⁶⁵ I. Kimchi and A. Vishwanath, *Phys. Rev. B* **89**, 014414 (2014).
⁶⁶ In the $\mathcal{H}-1$, the spiral-planes amongst sites in the honeycomb strips are slightly askew: bridging-sites share spiral-planes as do non-bridging-sites, but these two symmetry-inequivalent sites have spiral-planes that are slightly off-angle relative to each other (in a manner where the c -axis still lies in the spiral-planes).
⁶⁷ More precisely, the spiral-plane tilts slightly away from its related honeycomb-plane (in a manner where the c -axis still lies in the spiral-planes). The angle between a spiral-plane and its related honeycomb-plane is a monotonic function of $\varphi = \tan^{-1}(K/J) \in (-\pi, \pi)$: in the SP_{a-} phase, the angle is approximately 0 when φ is near $\pi/2$ and increases as φ moves towards π . In the SP_{b+} phase, the angle increases from approximately 0 when φ is closest to 0 and increases as φ decreases towards $-\pi/2$.
⁶⁸ The definition of the x, y, z axes in Ref. 47 and 48 is along the orthorhombic directions. In this work, we have labeled these as the $\hat{a}, \hat{b}, \hat{c}$ directions. Hence, we have replaced x, y, z with a, b, c in the basis vector notation to avoid confusion.
⁶⁹ S. Manni, S. Choi, I. I. Mazin, R. Coldea, M. Altmeyer, H. O. Jeschke, R. Valentí, and P. Gegenwart, *Phys. Rev. B* **89**, 245113 (2014).
⁷⁰ S. Manni, Y. Tokiwa, and P. Gegenwart, *Phys. Rev. B* **89**, 241102 (2014).
⁷¹ R. Coldea, talk at the SPOR13 conference held at MPIPKS, Dresden, 2013.